INTERNATIONAL JOURNAL FOR NUMERICAL METHODS IN FLUIDS
Int. J. Numer. Meth. Fluids 2009; **59**:657–676

Hybrid turbulence simulation of spray impingement cooling: The effect of vortex motion on turbulent heat flux

S. Kondaraju and J. S. Lee*, †

Department of Mechanical Engineering, Wayne State University, 5050 Anthony Wayne Dr. #2100, Detroit, MI 48202, U.S.A.

SUMMARY

Spray impingement has been a major interest of researchers in the areas of spray cooling, internal combustion, fire suppression and spray cooling, etc. for a long time. Numerous studies have been done in the area of spray cooling. Spray cooling with phase change takes advantage of relatively large amounts of latent heat and is capable of removing high heat fluxes from the surface, which has generated the interest of many researchers. In this paper, the turbulent characteristics of vapor formed during the spray impingement are studied. Water and gasoline are used in the numerical analysis of the two-phase spray impingement on a heated wall. Hybrid turbulence modeling was used for the analysis where the subgrid scale model was employed away from the wall and k–ε model was used near the wall. Gasoline, at 298 K, was sprayed on the heated wall, kept constant at 650 K. The surrounding temperature was maintained at 400 K at the start of the simulation. In case of water and gasoline at Reynolds number 2750, the heated wall was kept constant at 400 K and the surrounding temperature was maintained at 298 K at the start of the simulations. The nozzle diameter of 100 μm was used for this study, with the nozzle plate spacing ratio at 10. The spray was impinged on the flat plate at angles of 0, 15, and 30°. Root mean-squared velocities and turbulent heat flux were plotted in the water spray impingement for the different angles of impingement. The effect of turbulence on the heat transfer was observed. The effect of vortex motion on the turbulent heat flux values was analyzed using different Reynolds numbers of impingement and at different angles in case of gasoline. The turbulent heat flux attained the maximum values with high vortex formation. Upwash of fluid transported heat away from the wall, producing higher heat flux values in the region. Copyright © 2008 John Wiley & Sons, Ltd.

Received 11 October 2007; Revised 25 March 2008; Accepted 30 March 2008

KEY WORDS: injection cooling; vortex; turbulence; heat transfer; ALE; numerical method

---

*Correspondence to: J. S. Lee, Department of Mechanical Engineering, Wayne State University, 5050 Anthony Wayne Dr. #2100, Detroit, MI 48202, U.S.A.

†E-mail: joonlee@wayne.edu

Contract/grant sponsor: Wayne State University Institute for Manufacturing Research (IMR); contract/grant number: 3-36037
Contract/grant sponsor: Wayne State University Office of the Vice President for Research; contract/grant number: 1-76068

INTRODUCTION

Removal of large heat flux produced in power electronics and many other engineering applications has become a necessary condition and a barrier to growing technology. It is desirable to remove high rates of heat flux over a large area. Spray cooling has become an important tool in this case. To date, numerous experimental and theoretical studies have been carried out in the area of spray cooling and the effects of different parameters of spray impingement on heat removal rates. The effects of the spray nozzle, volumetric flux, the Sauter mean diameter of the spray, subcooling, and working fluid have been investigated. Several experiments have been performed in order to understand nucleate boiling and critical heat flux. Rini *et al.* [1] studied the heat transfer mechanism of spray cooling, which is associated with such phenomena as nucleate boiling due to surface nucleation and secondary nucleation, convection heat transfer, and direct evaporation from the surface of a liquid film. An experimental study of spray cooling to determine local quenching characteristics for various regimes of a water spray boiling curve was performed by Mudawar *et al.* [2]. Loureiro *et al.* [3] studied gasoline spray impacting perpendicular to a heated surface. The purpose of the study was to analyze the effects of the wall temperature, injection pressure, and pulse duration on the wall heat flux removed by spray cooling.

The above studies attempt to explain nucleate boiling and the effect of droplet impingement on heated walls. Kato *et al.* [4] suggested that thermal interactions between spray droplets and vapor during pre-impact have a significant influence on heat transfer in spray cooling. The effects that the mass flow rate [5–7], the impact angle [8], the surface roughness [9, 10], and reduced gravity [4, 11] may have on heat removal capacity in spray cooling have been investigated under transient conditions. Ortiz and Gonzalez [12] carried out spray cooling under steady-state conditions. They pointed out that high heat flux removal under steady-state conditions will facilitate system controllability.

To our knowledge, the effect of vapor formed during spray impingement has not been previously studied. Although the contribution of vapor to heat transfer is less than that of spray impingement on the whole, we were interested in understanding the behavior of vapor formed during spray impingement and its effects on heat transfer. The vortex motion formed by the vapor and its effect on heat transfer rate was studied. It was observed that the vapor formed during spray impingement has impinging jet characteristics. The studies of various researchers on jet impingement [13–39] have been utilized to study the behavior of heat transfer rate with the formation of vortex structures. Investigation of heat transfer in impinging jets of two-phase gas–particle suspensions [19–22] has been carried out. Shi *et al.* [22] developed a new Eulerian–Lagrangian model to predict the heat transfer in multiple-turbulent-slot impinging jets of dilute gas–particle suspensions by taking into account the conduction heat transfer due to particle–wall collisions. Gardon and Akfirat [23] investigated the local heat transfer characteristics of impinging two-dimensional and axis-symmetric air jets in the central zone around the stagnation point. They also studied the effect of free-stream turbulence on heat transfer augmentation. The effect of flow turbulence of the stagnation heat transfer of impinging jets issuing from a long straight pipe and from a convergent nozzle was studied by Hoogendoorn [24]. Obot *et al.* [25] and Popiel and Boguslawski [26] studied the effects of nozzle exit configurations and found that the nozzle exit configuration is the most important factor affecting heat transfer near the stagnation region. Lytle and Webb [27] measured the local heat transfer rate and flow structure at nozzle-to-plate spacing's less than one nozzle diameter and found peculiar behaviors that do not occur at higher spacing. Digital particle image velocimetry and laser-induced fluorescence have been developed [28, 29] for the simultaneous measurement of velocity and temperature. The role of coherent structures of turbulent flows in heat transfer was investigated. Heat transfer in a laminar impinging jet has been studied [30–33]. Chatterjee and Deviprasath [32] demonstrated that the off-stagnation point maxima of Nusselt number are entirely a consequence of upstream flow development because of vorticity diffusion. Numerical investigation of heat transfer rate using various k–ε models [34–37] has been carried out. Hosseinalipour and Mujumdar [35] compared the one standard and five low Reynolds number (LRN) versions of k–ε turbulence models to predict the heat transfer characteristics of confined turbulent single impinging and opposing slot jet flows. They also applied the Yap correction [35] to improve the prediction of downstream heat transfer of impinging jets, indicating that some of the models worked; however, those improvements were quite limited. Tzeng *et al.* [36] used one standard and seven LRN k–ε models to predict the heat transfer performance of multiple jets. Shuja *et al.* [38] used standard k–ε model, LRN k–ε model, and two Reynolds stress models to examine jet impingement on a surface having constant heat flux over a limited area. Cziesla *et al.* [39] studied the heat transfer from impinging slot jets using large-eddy simulations (LESs).

With this knowledge, we tried to explain the vortex formation of vapor formed from the liquid impingement and its relation to heat transfer rate using hybrid turbulence modeling. We investigated the turbulent properties of the vapor. We then tried to study the effect of vapor when fluid was sprayed at different angles and different Reynolds numbers. Cases simulated in this research are shown in Table I. The wall was initially heated for 10 ms and then the liquid at 298 K was sprayed onto the wall for the next 10 ms. Liquid was sprayed from a 100-μm nozzle on the heated wall, while the wall was maintained at a constant temperature. The surroundings are at a temperature of 400 K initially. The nozzle was at a distance of 1 mm from the heated wall and the surroundings were confined, as shown in Figure 1. The liquid impinges on the flat plate at angles of (θ) 0,

Table I. Cases simulated in this research.

	Reynolds number	Angle of impingement (deg.)	Wall temperature (K)	Surrounding temperature (K)
Water	2750	0	400	298
Gasoline	2750	0	400	298
Gasoline	4000	0, 15, 30	650	400
Gasoline	6000	0, 15, 30	650	400
Gasoline	7000	0, 15, 30	650	400

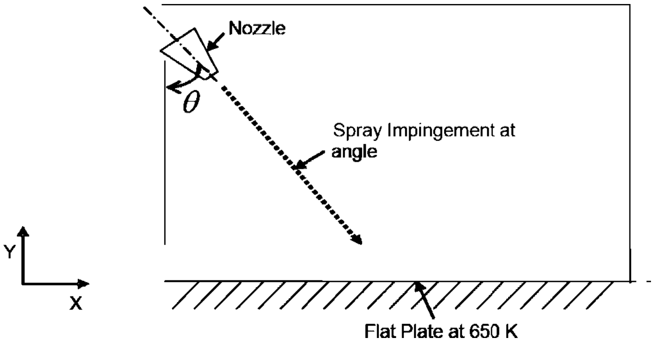

Figure 1. Schematic diagram of plane impingement and the coordinate axis.

15, and 30°. Angles are measured from the y-axis in the counter-clockwise direction as shown in Figure 1.

MATHEMATICAL FORMULATION

Governing equations—fluid phase

LES is now almost routinely used for the fundamental study of turbulence mechanics but the high demand of computational resources and the severe grid resolution in the near-wall region has been a major barrier to practical applications. To overcome such a barrier, the hybrid turbulence model has been implemented in the governing equations to represent the effects of turbulence in the present project. The governing equations for this model can be found in [40, 41]. The standard k–ε equations near the wall and a compressible LES formulation away from the wall were used in this research. The compressible LES formulation permitted the subgrid scale (SGS) turbulent Prandtl number to be computed dynamically. The complete formulation of source terms can be found in Amsden *et al.* [40] and Lee and Pletcher [42]:

$$\frac{\partial \rho k}{\partial t}+\nabla\cdot(\rho u k)=-\frac{2}{3}\rho k\nabla\cdot u+\sigma\nabla u+\nabla\cdot\left[\left(\frac{\mu}{Pr_k}\right)\nabla k\right]-\rho\varepsilon+\dot{W}^{\mathrm{s}} \tag{1}$$

and

$$\frac{\partial \rho\varepsilon}{\partial t}+\nabla\cdot(\rho u k)=-\left(\frac{2}{3}c_{\varepsilon_1}-c_{\varepsilon_3}\right)p\varepsilon\nabla\cdot u+\nabla\cdot\left[\left(\frac{\mu}{Pr}\right)\nabla\varepsilon\right]+\frac{\varepsilon}{k}[c_{\varepsilon_1}\sigma\nabla u-c_{\varepsilon_2}\rho\varepsilon+c_s\dot{W}^{\mathrm{s}}] \tag{2}$$

Equations (1) and (2) are standard k–ε equations with some added terms, which are used near the wall condition. The source term $-(\frac{2}{3}c_{\varepsilon_1}-c_{\varepsilon_3})\nabla\cdot u$ in the ε-equation accounts for length scale changes when there is velocity dilatation. Source terms involving the quantity $\dot{W}^{\mathrm{s}}$ arise due to the interaction with the spray. When the LES formulation is employed, the value is constrained to satisfy the inequality

$$\varepsilon\geqslant\left[\frac{c_\mu}{Pr_\varepsilon(c_{\varepsilon_2}-c_{\varepsilon_1})}\right]^{1/2}\frac{k^{3/2}}{L_{\mathrm{SGS}}} \tag{3}$$

where Pr_ε, c_μ, c_{ε_1}, and c_{ε_2} are constants whose values are determined from experiments and some theoretical considerations. L_{SGS} is the SGS length. Near the rigid walls, the boundary condition is applied such that Equation (3) is always satisfied. Thus, the standard k–ε equations are solved near the walls. Conditions applied near the wall are

$$\nabla k\cdot n=0 \tag{4}$$

$$\varepsilon=c_{\mu_\varepsilon}\frac{k^{3/2}}{y} \tag{5}$$

where k and ε are evaluated at a distance y from the wall and

$$c_{\mu_s}=\left[\frac{c_\mu}{Pr_\varepsilon(c_{\varepsilon_2}-c_{\varepsilon_1})}\right]^{3/2} \tag{6}$$

The compressible LES equations are obtained by spatial Favre filtering of the Navier–Stokes equations. The filter width is the grid scale and a box filter is used, since it is suitable for finite volume schemes [42–48]. Filtered LES equations are found to be consistent with the formulation [49, 50]

$$\frac{\partial \rho}{\partial t}+\nabla\cdot(\rho\overline{u})=\dot{\rho}^{\mathrm{s}} \tag{7}$$

$$\frac{\partial(\rho\overline{u})}{\partial t}+\nabla\cdot(\rho\overline{u}_i\overline{u}_j-\tau_{ij}+\tau_{ij}^{\mathrm{SGS}})=\dot{F}^{\mathrm{s}} \tag{8}$$

$$\frac{\partial(\rho\overline{u})}{\partial t}\nabla\cdot(\rho\overline{u}\overline{I})=-p\nabla\cdot\overline{u}+(1-A_0)\sigma\nabla\overline{u}-\nabla\cdot J+A_0\rho\varepsilon+\dot{Q}^{\mathrm{s}}+\phi^{\mathrm{SGS}}+\pi^{\mathrm{SGS}}+\theta^{\mathrm{SGS}} \tag{9}$$

where $\tau_{ij}=-p\delta_{ij}+\sigma_{ij}$. In these equations, τ_{ij}^{SGS}, ϕ^{SGS}, π^{SGS}, and θ^{SGS} represent the subgrid stress tensor, subgrid viscous work, subgrid velocity–pressure gradient correlation, and subgrid species mass flux, respectively [51].

Governing equations—droplet phase

Spray dynamic processes such as collision, transportation, evaporation, and breakup are considered in the spray equation using continuous droplet probability function f. The time evolution of continuous distribution function is given as follows:

$$\frac{\partial f}{\partial t}+\nabla_{x_{\mathrm{d}}}\cdot(f v_{\mathrm{d}})+\nabla_{v_{\mathrm{d}}}\cdot(fF)+\frac{\partial}{\partial T_{\mathrm{d}}}(f\dot{T}_{\mathrm{d}})=\dot{f}_{\mathrm{coll}} \tag{10}$$

where

$$\frac{\mathrm{d}x_{\mathrm{d}}}{\mathrm{d}t}=v_{\mathrm{d}},\quad \frac{\mathrm{d}v_{\mathrm{d}}}{\mathrm{d}t}=F,\quad \frac{\mathrm{d}r_{\mathrm{d}}}{\mathrm{d}t}=R=-\frac{\dot{m}_{\mathrm{d}}}{4\pi\rho_{\mathrm{d}}r_{\mathrm{d}}^2},\quad \frac{\mathrm{d}T_{\mathrm{d}}}{\mathrm{d}t}=\dot{T}_{\mathrm{d}} \tag{11}$$

The term $\dot{f}_{\mathrm{coll}}$ is a source term due to droplet collision. The acceleration of droplets is given as

$$\frac{\mathrm{d}v_{\mathrm{d}}}{\mathrm{d}t}=F=\frac{3}{8}\frac{\rho}{\rho_{\mathrm{d}}}\frac{|u+u'-v_{\mathrm{d}}|}{r_{\mathrm{d}}}(u+u'-v_{\mathrm{d}})C_D+g \tag{12}$$

$$\begin{aligned}C_D&=\frac{24}{Re_{\mathrm{d}}}\left(1+\frac{1}{6}Re_{\mathrm{d}}^{2/3}\right)\quad Re_{\mathrm{d}}<1000\\&=0.424\quad Re_{\mathrm{d}}>1000\end{aligned} \tag{13}$$

$$Re_{\mathrm{d}}=\frac{2\rho|u+u'-v_{\mathrm{d}}|r}{\mu_{\mathrm{air}}(\hat{T})} \tag{14}$$

where $\mu_{\mathrm{air}}(\hat{T})$ is the viscosity of the air given as $\mu_{\mathrm{air}}(\hat{T})=A_1\hat{T}^{3/2}/(\hat{T}+A_2)$. A_1, A_2 are constants and $\hat{T}$ is calculated as $\hat{T}=(T+2T_{\mathrm{d}})/3$.

The rate of droplet temperature change is determined by the energy balance equation

$$\rho_{\mathrm{d}}\tfrac{4}{3}\pi r^2 c_{\mathrm{l}}\dot{T}_{\mathrm{d}}-\rho_{\mathrm{d}}4\pi r^2 RL(T_{\mathrm{d}})=4\pi r^2 Q_{\mathrm{d}} \tag{15}$$

where c_{l} is the liquid specific heat and $L(T_{\mathrm{d}})$ is the latent heat of vaporization.

The heat conduction rate Q_d is given as

$$Q_{\mathrm{d}}=\frac{K_{\mathrm{air}}(\hat{T})(T-T_{\mathrm{d}})}{2r}Nu_{\mathrm{d}} \tag{16}$$

where

$$Nu_{\mathrm{d}}=(2.0+0.6Re_{\mathrm{d}}^{1/2}Pr_{\mathrm{d}}^{1/2})\frac{\ln(1+B_{\mathrm{d}})}{B_{\mathrm{d}}} \tag{17}$$

$$Pr_{\mathrm{d}}=\frac{\mu_{\mathrm{air}}(\hat{T})c_p(\hat{T})}{K_{\mathrm{air}}(\hat{T})} \tag{18}$$

$$K_{\mathrm{air}}(\hat{T})=\frac{K_1\hat{T}^{3/2}}{\hat{T}+K_2} \tag{19}$$

Boundary conditions

Velocity boundary conditions on rigid walls are introduced by imposing either the value of the velocity on the walls or the value of the wall stress $\sigma_{\mathrm{w}}=\sigma\cdot n$, where n is the unit normal to the wall. With the turbulent law-of-the-wall condition, the normal gas velocity is set equal to zero and the tangential velocity components are determined by matching to a logarithmic profile:

$$\begin{aligned}\frac{v}{u^*}&=\frac{1}{k\cdot\ln(c_{\mathrm{lw}}\zeta^{7/8})}+B \quad \text{for } \zeta>R_c\\ \frac{v}{u^*}&=\zeta^{7/8} \quad \text{for } \zeta<R_c\end{aligned} \tag{20}$$

where $\zeta=\rho y v/\mu_{\mathrm{air}}(T)$ is the Reynolds number based on the gas velocity relative to the wall, which is evaluated at a distance y from the wall, u^* is the shear speed, which is a function of the tangential components of the wall stress by

$$\sigma_{\mathrm{w}}-(\sigma_{\mathrm{w}}\cdot n)n=\rho(u^*)^2\frac{v}{v} \tag{21}$$

Temperature boundary conditions on rigid walls are introduced by specifying either the wall temperature or the wall heat flux $J_{\mathrm{w}}=-k\nabla T\cdot n$. For fixed temperature walls, using the turbulent law-of-the-wall condition, J_{w}, is determined from the modified Reynolds analogy formula

$$\begin{aligned}\frac{J_{\mathrm{w}}}{\rho u^* c_p(T-T_{\mathrm{w}})}&=\frac{1}{Pr_{\mathrm{l}}\dfrac{v}{u^*}} \quad \text{for } \zeta\leqslant R_c\\ \frac{J_{\mathrm{w}}}{\rho u^* c_p(T-T_{\mathrm{w}})}&=\frac{1}{Pr\left[\dfrac{v}{u^*}+\left(\dfrac{Pr_{\mathrm{l}}}{Pr}-1\right)\right]R_c^{1/2}} \quad \text{for } \zeta>R_c\end{aligned} \tag{22}$$

where T_{w} is the wall temperature and Pr_{l} is the Prandtl number of the laminar fluid. The temperature of the wall was set to be 650 K.

When a spray droplet impinges on a rigid wall, its velocity is set equal to zero. For the purpose of calculating heat transfer with the gas, Re_{d} is set equal to zero in Equation (17). It is assumed that there is no heat transfer between the droplet and wall.

NUMERICAL PROCEDURE

Implicit methods are used to differentiate the terms associated with acoustic pressure wave propagation and diffusion of mass, momentum, and energy equations. The flow field variables are then found by solving the implicit equations. A two-step iterative procedure, the SIMPLE method, is used to solve for the flow field variables. In step 1, the pressure field is predicted and the other flow quantities are solved using finite-difference equations that differentiate the diffusion terms implicitly. In step 2, the diffusion terms are frozen and the corrected pressure terms are solved using equations that differentiate the pressure terms implicitly. In the next phase, we calculate the convective transport associated with the fluid. This is accomplished in a subcycled explicit calculation using a time step, Δt_{c}, which is an integral submultiple of the main computational time step Δt. The convection scheme used in this study is a quasi-second-order upwind differencing. It must be mentioned that an arbitrary Eulerian–Lagrangian method is used in the numerical scheme. The Eulerian system is used to calculate the air properties, whereas fluid particle properties are calculated using the Lagrangian system.

The finite-difference approximations to the ordinary differential equations governing droplet trajectories and to the integrals that give the rates of mass, momentum, and energy exchange between the gas and spray are given below. The source term $\dot{\rho}^{\mathrm{s}}$ is defined as follows:

$$\dot{\rho}^{\mathrm{s}} = -\frac{1}{V^n \nabla t} \sum \left[N_p \rho_{\mathrm{d}} \frac{4}{3} \pi (r_p^A)^3 - (r_p')^3 \right] \tag{23}$$

The summation is over all particles located in the computational cell. The quantities N_p and r_p are values of the number and radius of the droplets in particle p, respectively, r_p^A is the droplet radius during the phase calculation where the physical effects of droplet collisions and evaporation are calculated.

The source term $\dot{Q}^{\mathrm{s}}$ is defined as follows:

$$\begin{aligned} \dot{Q}^{\mathrm{s}} = \frac{1}{V^n \nabla t} \sum \Big[& N_p \rho_{\mathrm{d}} \frac{4}{3} \pi (r_p^A)^3 I_{\mathrm{l}}(T_{\mathrm{d}}^A) - (r_p')^3 I_{\mathrm{l}}(T_{\mathrm{d}}') + (r_p^A)^3 (v_p^t - v_p') \cdot (v_p^t - u_{\mathrm{lms}}^n - u_p') \\ & + \frac{1}{2} [(r_p^A)^3 - (r_p')^3] (v_p^t - u_{\mathrm{lms}}^n)^2 \Big] \end{aligned} \tag{24}$$

where r_p', T_p', and v_p' are the radii, temperature, and velocities that are partially updated due to droplet collisions and breakups. The source term $\dot{W}^{\mathrm{s}}$ is defined as follows:

$$\dot{W}^{\mathrm{s}} = -\frac{1}{V^n \nabla t} \sum \left[N_p \rho_{\mathrm{d}} \frac{4}{3} \pi \rho_{\mathrm{d}} (r_p^A)^3 (v_p^t - v_p') \cdot u_p' \right] \tag{25}$$

Grid-independence test was carried out in our previous paper [52]. Axial root mean-squared (rms) velocity and average Nusselt number were computed and results obtained indicated that accurate and optimized results are obtained for the grid size of 30×30.

RESULTS AND DISCUSSION

Computational fluid dynamics validation for the code was carried out using the experimental data of Elison and Webb [53]. The numerical results are compared with two different cases. In the

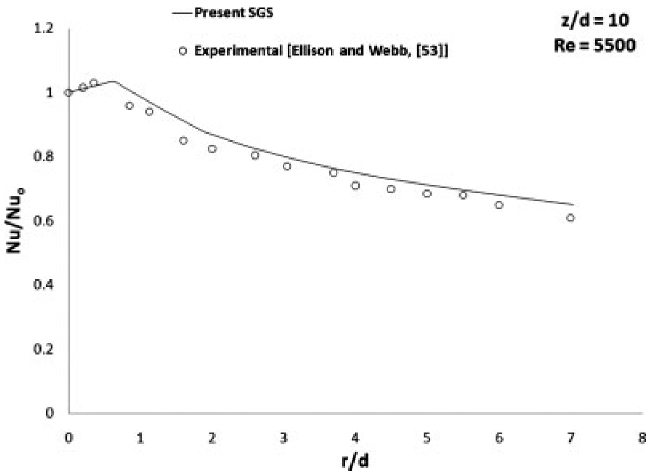

Figure 2. Radial variation of the normalized local Nusselt number for the free-surface jet configuration.

first case, the nozzle to plate spacing is $z/d = 10$. The Reynolds number of the jet at the exit is 5500. The jet impinges on a flat plate, with the diameter of the nozzle being $d = 0.32\,\mathrm{mm}$. The numerical results shown in Figure 2 are in good agreement with the experimental results. The radial variation of the normalized local Nusselt number, Nu/Nu_0, for the free-surface liquid jet configuration is shown in the figure. The simulated Nusselt number data were collected close to the wall at $y = 7.5\times10^{-5}\,\mathrm{m}$ from the plate. Maximum heat transfer occurs in the stagnation zone and falls off with the radial position. The heat transfer ratio falls to 60% of its value at the stagnation point at a radial distance of just six diameters.

In the second case, the nozzle-to-plate spacing used is $z/d = 1.5$. The Reynolds number of the jet at the exit in this case is 3400. The results are compared in Figure 3. Again, the radial variation of the local Nusselt number, Nu/Nu_0, is pronounced. The Nusselt number is calculated at $y = 1.5\times10^{-5}\,\mathrm{m}$. There is a slight discrepancy from the experimental results near the stagnation zone, but the variation is small enough to conclude that the numerical results match with the experimental results. Moving away from the stagnation point, the numerical results coincide with the experimental results. Comparing the experimental data and the current numerical data in Figures 2 and 3, numerical uncertainty of calculations from this code can be approximated around 6–8%.

Figure 4 shows the variation of rms velocities along the x-axis for different Reynolds numbers. The rms velocities are normalized by the injection velocity for a Reynolds number 4000 (V_{4000}). The v_{rms} values are observed to be high, approximately $y/D = 3$ in all three cases. The normal velocity fluctuation drops rapidly near the wall. However, the velocity fluctuation is observed to increase in the axial direction near the wall. Away from the wall, normal fluctuation is larger than axial fluctuation in all cases. This is a distinguishing property of jet impingements [54]. Although gasoline is sprayed onto the heated wall in the present case, the vapor formed can be said to follow jet impingement characteristics.

Figure 5 shows the helicity contour and the corresponding vorticity plot for the gasoline spray injection of Reynolds number 7000. It can be observed that helicity is sensitive to vortex formation of the fluid. The helicity contour shows maximum values at axial distances that are close to the

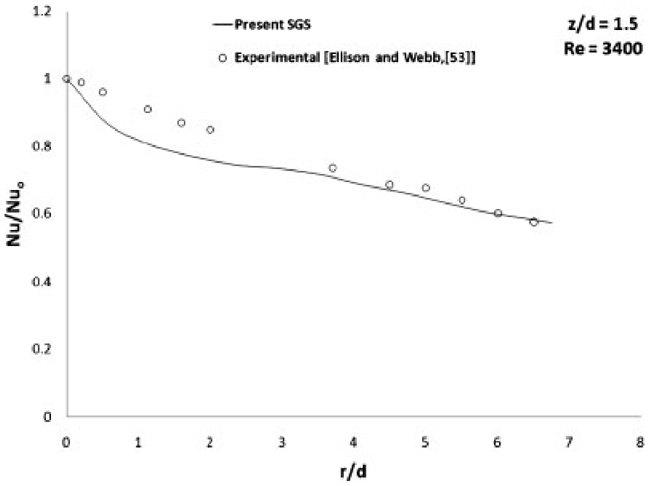

Figure 3. Radial variation of the normalized local Nusselt number for the free-surface jet configuration.

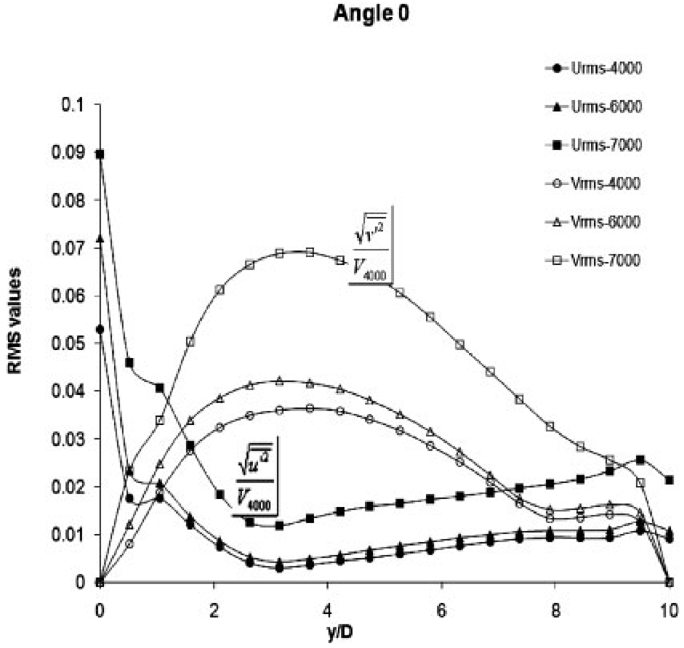

Figure 4. The rms velocity plots for 0° angle.

peaks of vortex plots at both 0.82 and 1.475 ms from the time of injection. This can be explained from the helicity formulation, which is given as He$=\overline{v}\cdot\overline{\omega}$, where $\overline{v}$ is the velocity vector and $\overline{\omega}$ is the vorticity vector. Hence, for the maximum values of vorticity, helicity can be expected to have

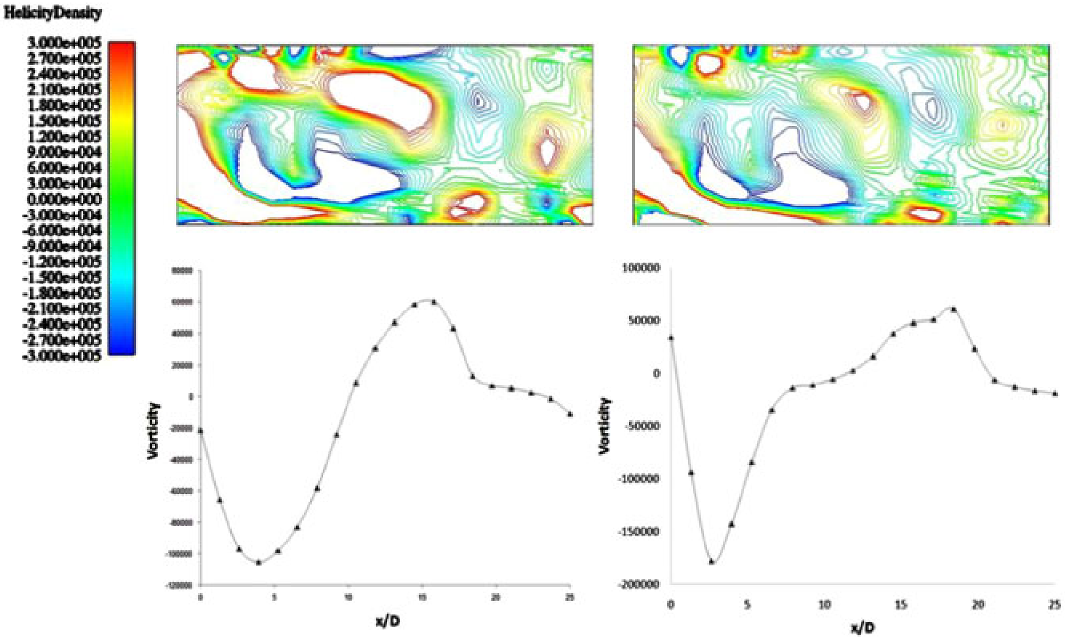

Figure 5. Helicity contour and corresponding vorticity plots.

larger values. This phenomenon can be clearly observed in Figure 6, where the helicity contour and the corresponding vorticity plots are shown for gasoline spray impingement of Reynolds number 4000. From the midpoint of the plate it can be observed that the helicity contour is fluctuating from minimum to maximum values. This change in contour values corresponds to the fluctuating values of vorticity, from x/D distances of 15. This phenomenon is observed at both 0.82 and 1.475 ms from the time of injection. Hence, Reynolds number 4000 is also seen to correlate between vorticity and helicity. Comparing Figures 5 and 6, it is observed that spray impingement with Reynolds number 7000 has shown greater helicity values compared with that of Reynolds number 4000. This can also be explained from the helicity formulation. Velocity vector is directly proportional to the helicity values and thus the increase in Reynolds number induces larger helicity values.

Turbulent structures and heat transfer

Correlation between turbulent structures and heat transfer near the flat plate is observed using the gasoline case of Reynolds number 7000. The contour plots of Nusselt, temperature, and vorticity are shown at $t = 4$ ms in Figure 7, along with the average plots of Nusselt, temperature, and vorticity. Higher vorticity regions in the contour plots can be related with high Nusselt values and low temperatures in the whole region. Similar conclusions can be made from the average plots of Nusselt, temperature, and vorticity, shown in the same figure.

Instantaneous turbulent heat flux contour plots and corresponding velocity and temperature fluctuations are shown in Figure 8, for the gasoline injection case of Reynolds number 7000. Maximum heat flux values are observed in the regions of ejection for $t = 0.6$ ms. Ejection occurs when values of $u' < 0$, v' and $T' > 0$ and fluid is said to be in a sweep motion when $u' > 0$, v' and $T' < 0$ [54, 55].

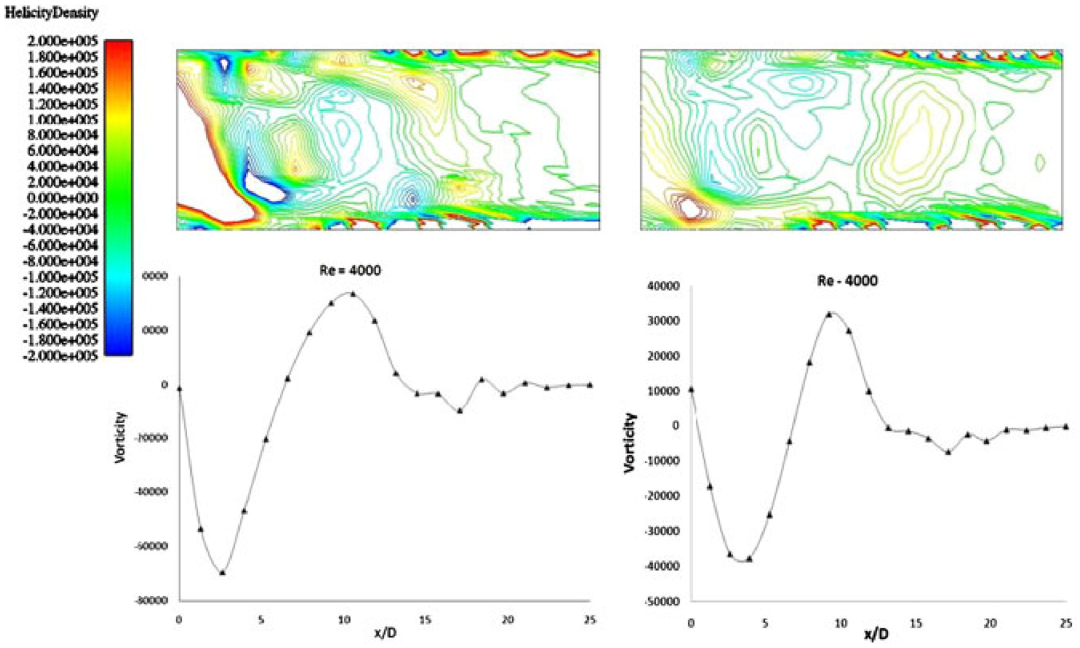

Figure 6. Helicity contour and corresponding vorticity plots.

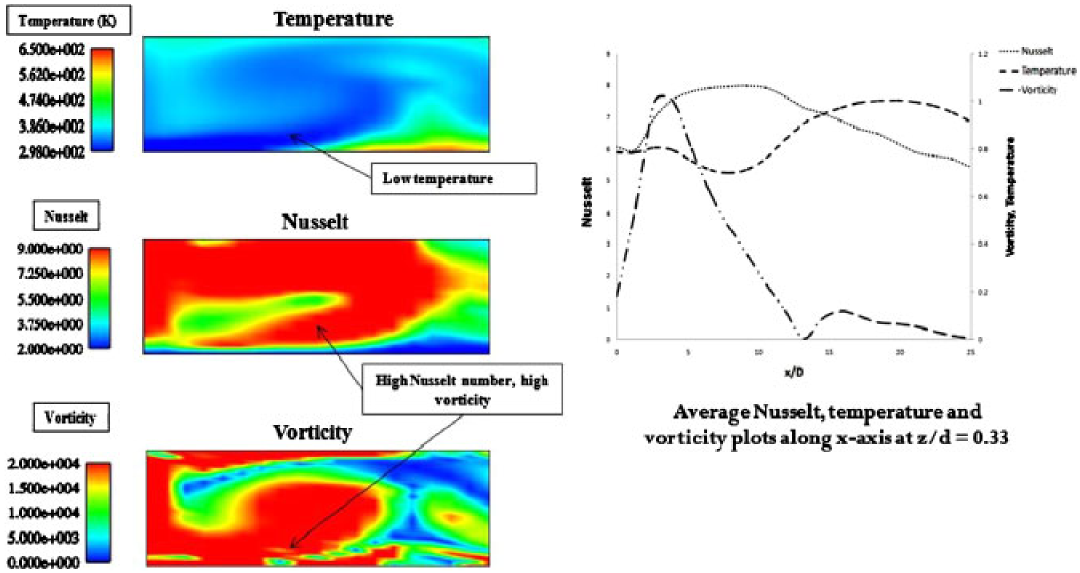

Figure 7. Instantaneous contour plots of Nusselt, temperature, and vorticity at $t=4$ ms and the corresponding averages plotted over the impinging time period on the right-hand side.

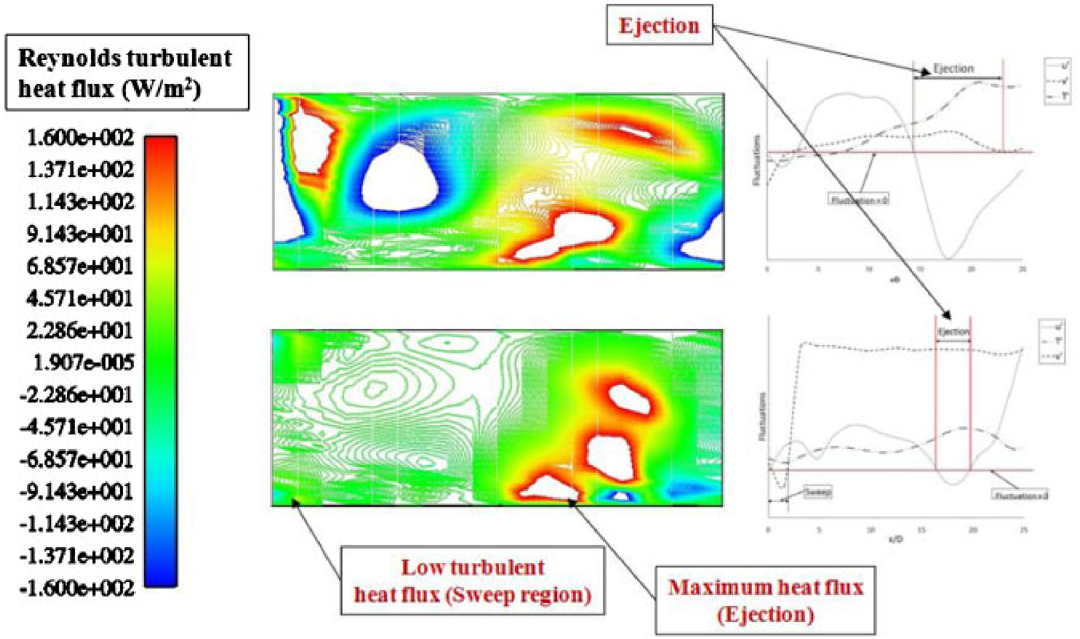

Figure 8. Instantaneous heat flux contour and corresponding velocity fluctuations for gasoline at Reynolds number 7000.

At $t=3.2$ ms, although the value of heat flux is not maximum in the ejection region, the values of heat flux are higher in the ejection region compared with that of the sweep region. It implies that the hot fluid ejection is greater compared with the down sweep motion of the cold fluid. Results in this section indicate the higher heat transfer rate observed in the region of predominant turbulence activity.

Water and gasoline

The effect of vapor formation during the injection of both water and gasoline is discussed in this section. Reynolds number 2750 is used for both cases. In Figure 9 instantaneous contour plots of turbulent heat flux and corresponding velocity and temperature fluctuations are shown for water and gasoline cases, at $t=0.6$ and 3.2 ms. The water injection case is shown on the left-hand side of the figure and the gasoline injection case is shown on the right-hand side. Low turbulent heat flux values are predominantly observed in the water spray case. This can be explained from the negative turbulent activity occurring away from the stagnation point. From the plots of velocity fluctuations, it is observed that $u', v'<0$ or $u', v'>0$ for most of the region away from the stagnation point. This implies a negative turbulence activity where low-speed fluids enter the region and high-speed fluids move away from the region. In case of gasoline at Reynolds number 2750, a similar phenomenon is observed for most of the region. However, due to the lower spread of sweep regions, the heat flux values are higher in this case compared with that of the water spray case. This can be confirmed from Figure 10 where temperature contour plots are shown for water and

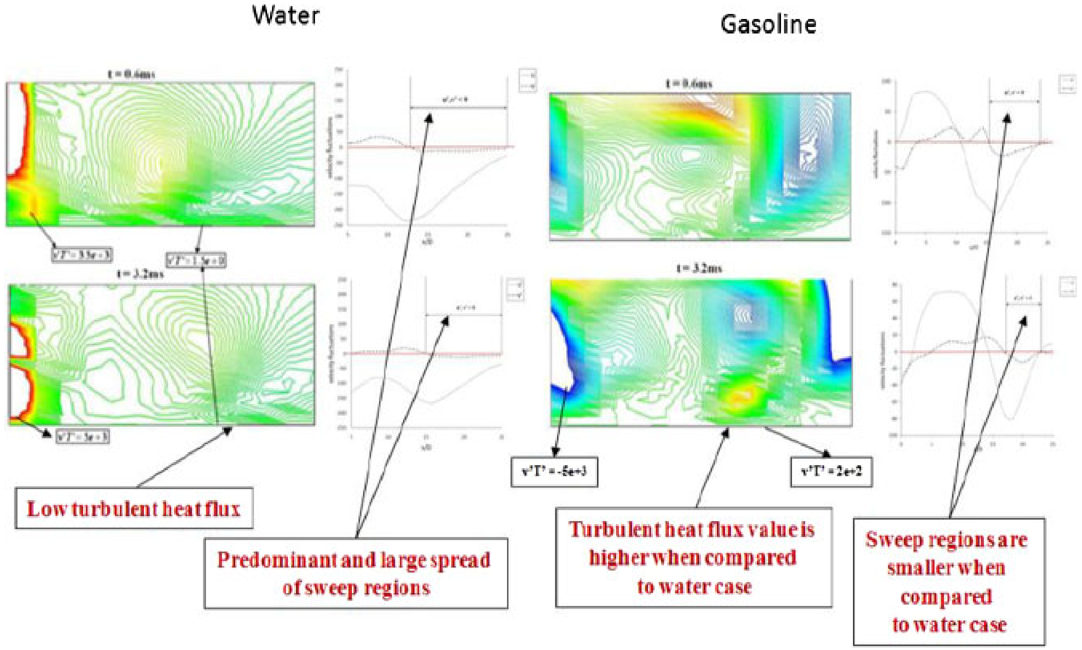

Figure 9. Instantaneous heat flux contour and corresponding velocity fluctuations for water and gasoline at Reynolds number 2750.

gasoline cases at Reynolds number 2750. At the same instantaneous positions, the gasoline case shows lower temperatures near the wall region compared with that of the water case.

Comparison

Heat transfer rates are compared at different angles 0, 15, and 30° for the gasoline spray impingement. Figure 11 shows the temperature contour plots at $t = 0.6$ ms, and average temperature profiles near the flat plate, at different angles of impingement for the Reynolds number of 7000. Contour plots show the large spread of low temperature values at angle 0°. Although contour plots show higher temperatures away from the stagnation zone at angle 0°, the average temperature profile indicates that over a period of time temperature values at angle 0° are lower when compared with the other two angles. To understand the reason behind this effect, Reynolds normal heat flux contour plots are shown at $t = 0.6$ ms at all three angles of impingement in Figure 12. Black arrows imposed on the contour plots show the velocity vectors. High axial velocities are observed at angles 15 and 30°. Fluid quickly moves away from the stagnation point and vorticity occurs either away from the stagnation point or away from the plate in the y-direction, thus making the turbulence formed ineffective to reduce heat transfer near the plate. This phenomenon can be observed from the Reynolds heat flux contour plot, where maximum heat flux values occur either near the confined wall or away from the plate, at angles 15 and 30°. But in the case of spray impingement at the angle of 0°, higher turbulence activity occurs near the stagnation point and close to the flat plate. This increases the heat transfer rate at 0° angle and hence reduces the overall temperature close to the flat plate.

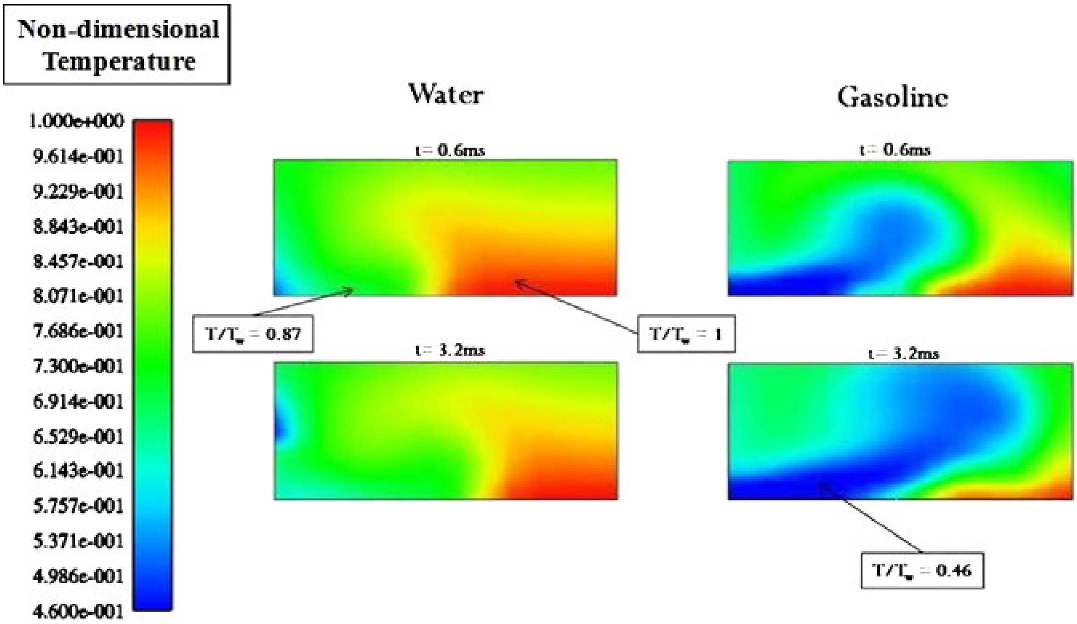

Figure 10. Temperature contour plots of water and gasoline at Reynolds number 2750.

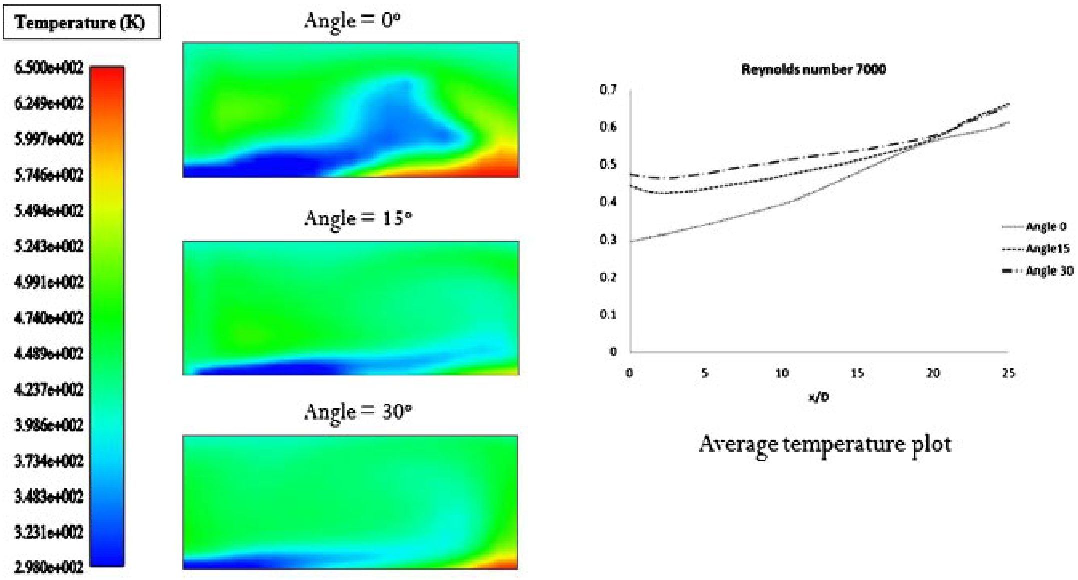

Figure 11. Temperature contour plots and average temperature profile for angles of impingement of 0, 15, and 30°.

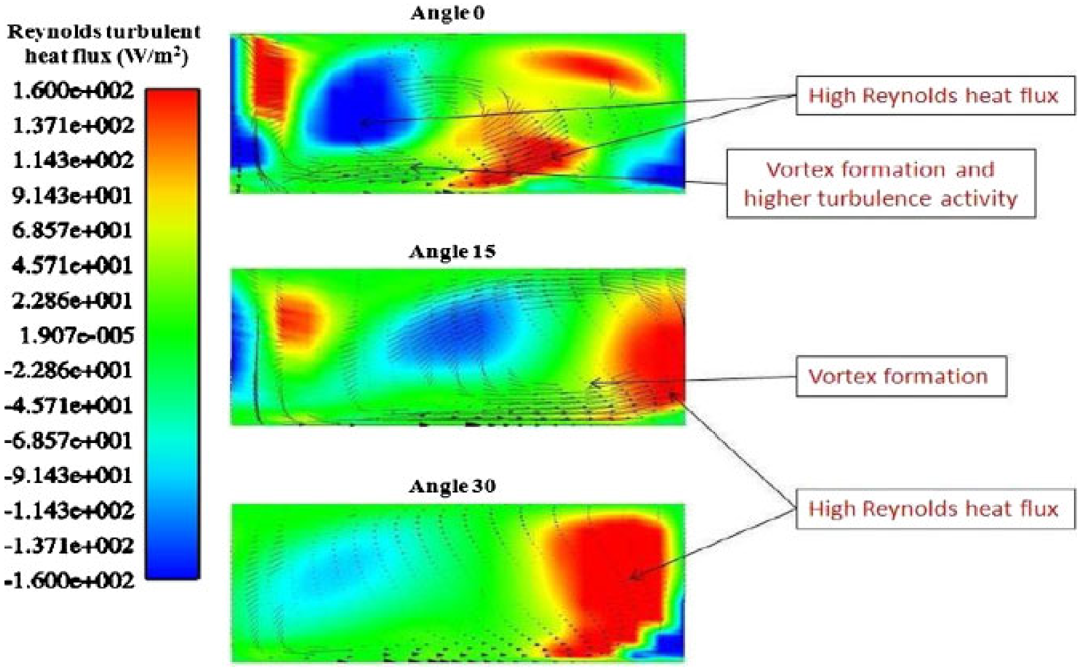

Figure 12. Velocity vector superimposed on the Reynolds heat flux contour plot for angles of impingement of 0, 15, and 30°.

However, at the lower Reynolds numbers of impingement, both 15 and 30° angles have lower average temperature when compared with 0° angle as shown in Figures 13 and 14. Away from the stagnation point, the temperature rises steeply for both Reynolds numbers 4000 and 6000 when the angle of impingement is 0°. Lower axial velocity formed at the 0° angle of impingement prevents fluid from reaching the regions away from the stagnation zone, thus reducing the heat transfer in those regions.

CONCLUSION

In this paper, a study was performed on the vapor formed during spray impingement on a heated wall using numerical simulation. Turbulent characteristics of vapor were determined using a hybrid turbulence model, which uses the LES formulation away from the wall and a k–ε model close to it. The heat transfer characteristics were observed when the spray impinges on a heated wall at different Reynolds numbers and at different angles.

Simulations were performed on gasoline spray impingement and water spray impingement, and turbulent heat flux values were analyzed. Turbulence was previously reported to play an important role in heat transfer characteristics since it enhances the mixing of fluid in the core region with fluid in the wall region. The objective here is to perform an analysis of the influence of the turbulent characteristics of vapor formed during the spray impingement, on heat transfer over a flat plate. Turbulent structures were analyzed, using rms velocity plots and the helicity contour

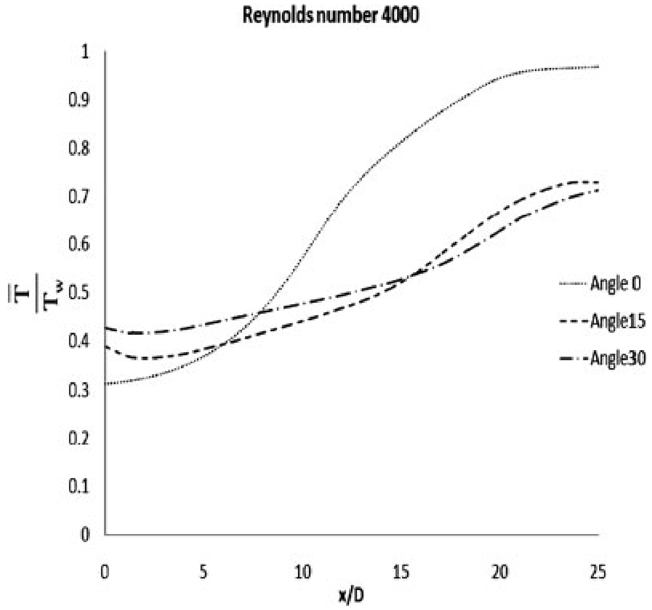

Figure 13. Average temperature profile for different angles of impingement at Reynolds number 4000.

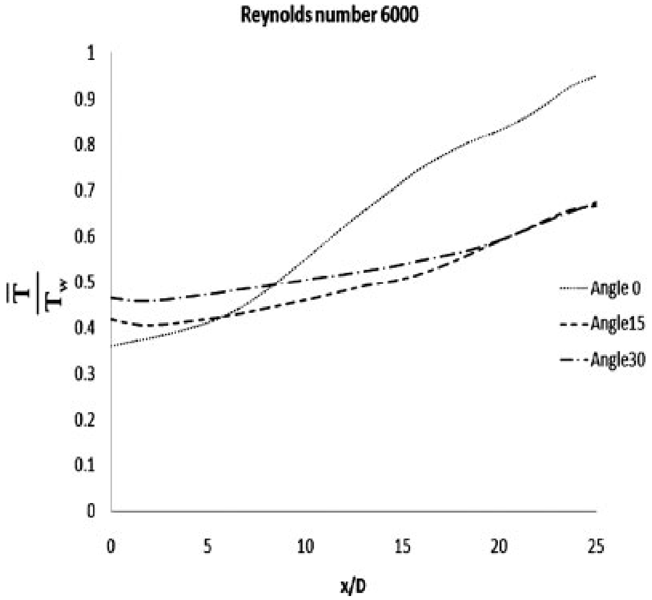

Figure 14. Average temperature profile for different angles of impingement at Reynolds number 6000.

and the corresponding vorticity plots, for gasoline cases. The turbulent properties were observed to be higher for higher Reynolds numbers of injection. Then the relation between vortex motion and heat transfer was investigated for the vapor formed during spray impingement. The results showed that the turbulent heat flux values were greater at the point of vortex formation. High heat flux values were observed when the upwash of fluid transported heat from the wall.

Reynolds normal heat flux values were compared for gasoline cases of Reynolds numbers 2750 and 7000 and for the water case of Reynolds number 2750. Negative turbulent activity was observed to be predominant in both cases of Reynolds number 2750 but water case showed large spread of sweep regions and hence low value of heat transfer when compared with gasoline at Reynolds number 2750, whereas gasoline injection of Reynolds number 7000 shows higher turbulent activity and thus greater heat transfer rates. Heat transfer rates were compared for different angles of impingement for gasoline at Reynolds numbers 7000, 6000, and 4000. A 0° impingement showed higher heat transfer rates when compared with other two angles at Reynolds number 7000. However, at Reynolds numbers 6000 and 4000, 15 and 30° angles were observed to be more effective. Away from the stagnation zone, 0° angle of impingement has very low heat transfer, which can be concluded from the high average temperature observed in that region.

NOMENCLATURE

D	diameter of the nozzle
D	diffusion coefficient
g	gravitational acceleration
I	specific internal energy
J	heat flux vector
k	turbulent kinetic energy
Nu	local Nusselt number
P	fluid pressure
Pr	Prandtl number
Re	Reynolds number
T	temperature of the fluid
$\overline{T}$	time-averaged temperature
T'	temperature fluctuation
u, v	gas velocities in the x- and y-directions
V	velocity at the nozzle exit
u_{rms}, v_{rms}	rms values of velocity fluctuation in the x- and y-directions
u', v'	velocity fluctuations in the axial and vertical directions
ε	dissipation rate of turbulent kinetic energy
ρ	total mass density
μ	viscosity
σ_{w}	wall stress

Subscript

m	species
0	stagnation point quantity
rms	root mean square

DOI: 10.1002/fld

SGS	subgrid scale contribution
w	wall quantity

Superscript

s	terms for spray interactions
−	resolved or large-scale component of filtered quantity

Abbreviations

CFD	computational fluid dynamics
LES	large-eddy simulation
SGS	subgrid scale

ACKNOWLEDGEMENTS

The current research was partially supported by the Wayne State University Institute for Manufacturing Research (IMR) under the grant 3-36037 and by the Wayne State University Office of the Vice President for Research under the grant 1-76068.

REFERENCES

1. Rini DP, Chen RH, Chow LC. Bubble behavior and nucleate boiling heat transfer in saturated FC-72 spray cooling. *Journal of Heat Transfer* 2002; **124**:63–72.
2. Mudawar I, Estes KA. Optimizing and predicting CHF in spray cooling of a square surface. *Journal of Heat Transfer* (ASME) 1996; **118**:672–679.
3. Loureiro HM, Panao MRO, Moreira ALN. Simultaneous measurements of droplet characteristics and surface thermal behavior to study spray cooling with pulsed sprays. *Twelfth International Symposium on Applications of Laser Techniques to Fluid Mechanics*, Lisboa, 2004.
4. Kato M, Abe Y, Oka T, Mori YH, Nagashima A. Spray cooling under reduced gravity conditions. *Journal of Heat Transfer* (ASME) 2001; **123**:309–318.
5. Halvorson PJ, Carson RJ, Jeter SM, Abdel-Khalik SI. Critical heat flux limits for a heated surface impacted by a stream of liquid droplets. *Journal of Heat Transfer* 1994; **116**:679–685.
6. Webb BW, Queiroz M, Oliphant KN, Bonin MP. Onset of dry-wall heat transfer in low-mass-flux spray cooling. *Experimental Heat Transfer* 1992; **5**:33–92.
7. Yao SC, Chio KJ. Heat transfer experiments of mono-dispersed vertically impacting sprays. *International Journal of Multiphase Flow* 1987; **13**:639–648.
8. McGinnis FK, Holman JP. Individual droplet heat-transfer rates for splattering on hot surfaces. *International Journal of Heat and Mass Transfer* 1969; **12**:95–108.
9. Pais MR, Chow LC, Mahefkey ET. Surface roughness and its effects on the heat transfer mechanism in spray cooling. *Journal of Heat Transfer* 1992; **114**:211–219.
10. Bernardin JD, Stebbins CJ, Mudawar I. Effects of surfaces roughness on water droplet impact history and heat transfer regime. *International Journal of Heat and Mass Transfer* 1997; **40**:73–88.
11. Qiao YM, Chandra S. Boiling of droplets on a hot surface in low gravity. *International Journal of Heat and Mass Transfer* 1996; **39**:1379–1393.
12. Ortiz L, Gonzalez JE. Experiments on steady-state high heat fluxes using spray cooling. *Experimental Heat Transfer* 1999; **12**:215–233.
13. Chochua G, Shyy W, Thakur S, Brankovic A, Lienau J, Porter L, Lischinsky D. A computational and experimental investigation of turbulent jet and crossflow interaction. *Numerical Heat Transfer*, *Part A*: *Applications* 2000; **38**(6):557–572.
14. Chattopadhyay H, Saha SK. Numerical investigations of heat transfer over a moving surface due to impinging knife jets. *Numerical Heat Transfer*, *Part A*: *Applications* 2001; **39**(5):531–549.
15. Aissia HB, Zaouali Y, El Golli S. Numerical study of the influence of dynamics and thermal exit conditions on axisymmetric laminar bouyant jet. *Numerical Heat Transfer*, *Part A*: *Applications* 2002; **42**:427–444.

16. Hatem SM, El Golli MS, Le Palec G, Bournot P. Numerical study of a heated pulsed axisymmetric jet in laminar mode. *Numerical Heat Transfer*, *Part A*: *Applications* 2003; **43**:409–429.
17. Bula AJ, Rahman MM, Leland JE. Numerical modeling of conjugate heat transfer during impingement of free liquid issuing from a slot nozzle. *Numerical Heat Transfer*, *Part A*: *Applications* 2000; **38**:45–66.
18. Tong Y. A numerical study on the hydrodynamics and heat transfer of a circular liquid jet impinging onto a substrate. *Numerical Heat Transfer*, *Part A*: *Applications* 2003; **44**:1–19.
19. Mashayek F, Taulbee DB. Turbulent gas–solid flows, part I: direct simulations and Reynolds stress closures. *Numerical Heat Transfer*, *Part B*: *Fundamentals* 2002; **41**:1–29.
20. Mashayek F, Taulbee DB. Turbulent gas–solid flow, part II: explicit algebraic models. *Numerical Heat Transfer*, *Part B*: *Fundamentals* 2002; **41**:31–52.
21. Nguyen AV, Fletcher CAJ, Tu JY. CFD study of the heat transfer between a dilute gas particle suspension flow and an obstruction. *Numerical Heat Transfer*, *Part A*: *Applications* 1999; **35**:537–551.
22. Shi YL, Mujumdar AS, Ray MB. Heat transfer in a multiple-turbulent-slot impinging jets of gas–particle suspensions. *Numerical Heat Transfer*, *Part A*: *Applications* 2005; **47**:147–164.
23. Gardon R, Akfirat JC. The role of turbulence in determining the heat transfer characteristics of impinging jets. *International Journal of Heat and Mass Transfer* 1965; **8**:1261–1272.
24. Hoogendoorn CJ. The effects of turbulence on heat transfer at a stagnation point. *International Journal of Heat and Mass Transfer* 1975; **18**:597–605.
25. Obot NT, Majumdar AS, Douglas WJM. The effect of nozzle geometry on impingement heat transfer under a round turbulent jet. *ASME Paper 79-WA/DT-53*, 1979.
26. Popiel CO, Boguslawski L. Effect of flow structure on the heat or mass transfer on a flat plate in impinging round jet. *Proceedings of the 2nd U.K. National Conference on Heat Transfer*, University of Strathclyde, U.K., vol. 1, 1988; 663–685.
27. Lytle D, Webb BW. Air jet impingement heat transfer at low nozzle–plate spacing. *International Journal of Heat and Mass Transfer* 1994; **37**:1687–1697.
28. Sakakibara J, Hishida K, Maeda M. Measurements of thermally stratified pipe flow using image-processing techniques. *Experiments in Fluids* 1993; **16**:82–96.
29. Sakakibara J, Hishida K, Maeda M. Quantitative visualization of convective heat transfer near the stagnation region of an impinging jet. *Fluids Engineering Division* (ASME) 1993; **172**:93–99.
30. Chattterjee A, Dhingra SC, Kapur SS. Laminar impinging jet heat transfer with a purely viscous inelastic fluid. *Numerical Heat Transfer*, *Part A*: *Applications* 2002; **42**:757–775.
31. Aldabbagh LBY, Sezai I. Numerical simulation of three-dimensional laminar, square twin jet impingement on a flat plate, flow structure and heat transfer. *Numerical Heat Transfer*, *Part A*: *Applications* 2002; **41**:835–850.
32. Chatterjee A, Deviprasath LJ. Heat transfer in a confined laminar axisymmetric impinging jets at small nozzle-plate distances: the role of upstream vorticity diffusion. *Numerical Heat Transfer*, *Part A*: *Applications* 2001; **39**:777–800.
33. Besserman DL, Ramadhyani S, Incropera FP. Numerical simulations of laminar flow and heat transfer for liquid jet impingement cooling of a circular heat source with annular collection of spent fluid. *Numerical Heat Transfer*, *Part A*: *Applications* 1991; **20**:263–278.
34. Seyedein SH, Hasan M, Mujumdar AS. Turbulent flow and heat transfer from confined multiple impinging slot jets. *Numerical Heat Transfer*, *Part A*: *Applications* 1995; **27**:35–51.
35. Hosseinalipour SM, Mujumdar AS. Comparative evaluation of different turbulence models for confined impinging and opposing jet flows. *Numerical Heat Transfer*, *Part A*: *Applications* 1995; **28**:647–666.
36. Tzeng PY, Soong CY, Hsieh CD. Numerical investigation of heat transfer under confined impinging turbulent slot jets. *Numerical Heat Transfer*, *Part A*: *Applications* 1999; **35**:903–924.
37. El-Gabry LA, Kaminski DA. Numerical investigation of jet impingement with cross flow-comparison of Yang–Shih and standard k–ε turbulence models. *Numerical Heat Transfer*, *Part A*: *Applications* 2005; **47**:441–469.
38. Shuja SZ, Yilbas BS, Budair MO. Gas jet impingement on a surface having a limited constant heat flux area: various turbulence models. *Numerical Heat Transfer*, *Part A*: *Applications* 1999; **36**:171–200.
39. Cziesla T, Tandagon E, Mitra NK. Large-eddy simulation of heat transfer from impinging slot jets. *Numerical Heat Transfer*, *Part A*: *Applications* 1997; **32**:1–17.
40. Amsden AA, Ramshaw JD, Cloutman LD, O'Rourke PJ. KIVA: a comprehensive model for 2D and 3D engine simulations. *SAE Technical Paper 850554*, 1985.
41. Tev KG, Timothy EC, Norman C. A numerical and experimental study of spray dynamics in a simple throat model. *Aerosol Science and Technology* 2002; **36**:18–38.

42. Lee JS, Pletcher RH. LES of variable property turbulent flow in horizontal and vertical channels with buoyancy and heat transfer effects. *Journal of Mechanical Engineering Science* 2007; **221**:429–441.
43. Lee JS, Xu X, Pletcher RH. Large eddy simulation of heated vertical annular pipe flow in fully developed turbulent mixed convection. *International Journal of Heat and Mass Transfer* 2004; **47**:437–446.
44. Lee JS, Xu X, Pletcher RH. Numerical study of the effects of rotation on heat transfer in channels with and without ribs. *International Journal of Heat and Mass Transfer* 2004; **47**:4673–4684.
45. Lee JS, Xu X, Pletcher RH. Large eddy simulation of the effects of inner wall rotation on heat transfer in annular turbulent flow. *Numerical Heat Transfer*, *Part A*: *Applications* 2004; **46**:323–341.
46. Lee JS, Xu X, Pletcher RH. Effects of wall rotation on heat transfer to annular turbulent flow: outer wall rotating. *Journal of Heat Transfer* 2005; **127**:830–838.
47. Xu X, Lee JS, Pletcher RH, Shehata M, McEligot DM. Large eddy simulation of turbulent forced gas flows in vertical pipes with high heat transfer rates. *International Journal of Heat and Mass Transfer* 2004; **47**:4113–4123.
48. Xu X, Lee JS, Pletcher RH. A compressible finite volume formulation for large eddy simulation of turbulent pipe flows at low Mach number in cartesian coordinates. *Journal of Computational Physics* 2005; **203**:22–48.
49. Kim WW, Menon S, Mongia HC. Numerical simulations of reacting flows in a gas turbine combustor. *Combustion Science and Technology* 1999; **143**:25–62.
50. Menon S. Subgrid combustion modeling for large-eddy simulations. *International Journal of Engine Research* 2000; **1**:209–227.
51. Sone K, Menon S. Effect of subgrid modeling on the in-cylinder unsteady mixing process in a direct injection engine. *Journal of Engineering for Gas Turbines and Power* 2003; **125**:435–443.
52. Kondaraju S, Lee JS. Hybrid turbulence modeling of liquid spray impingement on a heated wall with arbitrary Lagrangian–Eulerian method. *Numerical Heat Transfer*, *Part A*: *Applications* 2007; **52**(12).
53. Elison B, Webb W. Local heat transfer to impinging liquid jets in the initially laminar, transitional, and turbulent regimes. *International Journal of Heat and Mass Transfer* 1994; **37**:1207–1216.
54. Sakakibara J, Hishida K, Maeda M. Vortex structure and heat transfer in the stagnation region of an impinging plane jet (simultaneous measurements of velocity and temperature fields by digital particle image velocimetry and laser-induced fluorescence). *International Journal of Heat and Mass Transfer* 1997; **40**:3163–3176.
55. Panton RL. *Incompressible Flow* (2nd edn). Wiley: New York, 1996; 789–791.